100 Gbps Radio Over Free Space Communication Using Space Diversity Reception Based on Photodetector Array

Yunjie Yan, Joris Van Kerrebrouck, Nishant Singh, Mingxiang Yang, Yutong Liu, Shiyuan Zhao, Yiying Gu, Mingshan Zhao, and Geert Morthier

***Abstract*—With the rapid advancement of optical communication technology, radio over free space optical (RoFSO) communication has demonstrated considerable potential in communication applications due to its high bandwidth and low latency characteristics. A free space optical (FSO) receiver with high optical alignment robustness configured by a single optical lens is presented. The 10-element photodetector array (PDA) offers an expansive active detection area with a responsivity of 1.01 A/W at 1550 nm wavelength. In a 0.35 m FSO demonstration, the z-axis optical alignment tolerance on the condenser lens is evaluated to be as large as 65 μm without crosstalk, demonstrating the robustness of the receiver design. The multiple output signals from the receiver are used in space diversity. A receiving rate of up to 100 Gbps (10 $\times$ 10 Gbps) NRZ with a bit error rate (BER) below 10^{-12} is demonstrated after 25 km long distance single mode fiber (SMF) transmission. The system design and alignment tolerance without a mechanical beam tracking system are presented which verifies its feasibility in a high speed RoFSO communication system. It further demonstrates the potential for applications in space division multiplexing (SDM) systems.**

***Index Terms*—Radio over free space transmission, photodetector array, space division reception.**

I. Introduction

THE exponential growth of global data traffic, driven by emerging applications such as artificial intelligence (AI) [1], high definition data streaming [2] and the Internet of Things (IoT) [3], has created unprecedented demand for higher transmission capacity in wireless communication systems. To accommodate heavy data traffic, wireless technologies [4], [5] require ultra high data rates (~20 Gbps), low latency (<1 ms) and massive connectivity [6]. Space division multiplexing (SDM) has emerged as a key technology to address the challenges by exploiting parallel spatial channels in multicore fibers (MCFs) [7] or few mode fibers (FMFs) [8] and thus simultaneous data streams are supported and transmission capacity is multiplied. A critical component in SDM systems is the receiver, which must efficiently demultiplex and detect multiple spatial channels simultaneously.

Conventional implementations require complex fiber-splicing processes to separate signals from multicore or multimode fibers into individual single mode fibers (SMFs), each connected to a discrete photodetector [9]. The method introduces significant challenges including increased system complexity, higher insertion losses, larger footprint and elevated costs, particularly as the number of spatial channels increases [10], [11].

To overcome the limitations of conventional detection methods, alternative techniques have been explored. Visible light communication (VLC) [12] using LED-based systems [13], [14] offers a wireless alternative with moderate data rates (~ 1 Gbps), but LED bandwidth constraints limit performance. Free space optical (FSO) systems achieve high speeds through precision beam tracking and spatial multiplexing, which enabled transmission rates exceeding 100 Gbps [15]. Since light has a higher frequency than microwaves, it can carry much more information [16], [17]. In the Radio over free space (RoFSO) communication system [18], it can enable flexible, high speed and cable free interconnections with aggregate rates above 400 Gbps through multiple parallel spatial channels [19]. Such systems have demonstrated 1-m free space links with QPSK, 4APSK and 8QAM optical signals at 1 Gbaud [20].

As a key component of RoFSO systems, photodetector arrays (PDAs) offer an elegant solution. By integrating multiple photodetector elements in a planar array, PDAs can directly couple with spatial channels without intermediate fan-out devices [21]. Each element detects a distinct spatial channel, enabling parallel data reception, which become increasingly impractical with fan-out devices at higher core counts. Despite these promising developments, several challenges remain in optimizing PDA performance. These include achieving high responsivity and bandwidth for each photodetector element,

Received 26 November 2025; revised 26 January 2026; accepted 11 February 2026. Date of publication 20 February 2026; date of current version 2 May 2026. This work was supported in part by the BOF fund of Ghent University, the Program of China Scholarship Council under Grant 202306060161 and in part by the Fundamental Research Funds for the Central Universities. *(Corresponding author: Yiying Gu.)*

Yunjie Yan is with the School of Optoelectronic Engineering and Instrumentation Science, Dalian University of Technology, Dalian 116024, China, and also with the Photonics Research Group, INTEC Department, Ghent University, 9052 Ghent, Belgium.

Joris Van Kerrebrouck and Nishant Singh are with the IDLab, INTEC Department, Ghent University, 9052 Ghent, Belgium.

Mingxiang Yang, Yutong Liu, Shiyuan Zhao, Yiying Gu, and Mingshan Zhao are with the School of Optoelectronic Engineering and Instrumentation Science, Dalian University of Technology, Dalian 116024, China (e-mail: yiyinggu@dlut.edu.cn).

Geert Morthier is with the Photonics Research Group, INTEC Department, Ghent University, 9052 Ghent, Belgium.

Color versions of one or more figures in this article are available at https://doi.org/10.1109/JLT.2026.3666655.

Digital Object Identifier 10.1109/JLT.2026.3666655

minimizing crosstalk between adjacent elements, ensuring uniform performance across the array and developing cost effective fabrication processes compatible with existing photonic integration platforms. Addressing these challenges is essential for realizing the full potential of PDA-enabled SDM systems using space division reception in next-generation optical networks. In this work, we focus on the development and characterization of novelty PDA technologies for RoFSO applications, with emphasis on high speed operation, high responsivity and compatibility for scalable RoFSO communication systems. We combine direct PDA based space diversity reception with a hybrid fiber and FSO transmission. By integrating 25 km SMF analog fiber transmission with a 0.35 m free space optical link, we target practical deployment scenarios with both fiber infrastructure and wireless flexibility. We demonstrate 100 Gbps (10 $\times$ 10 Gbps) transmission with direct free space coupling to a novel high speed PDA which was reported in our previous work [22] and features 50 μm photosensitive elements.

II. Free Space Transmission Simulation

To realize a simple, low cost FSO receiver for short range wireless links, we adopt a streamlined architecture consisting of a PDA and a condenser lens, without any active optical beam tracking module. The PDA integrates 10 elements, each with a 50 μm photosensitive diameter. With this arrangement, tight pointing control is unnecessary, as long as the received beam footprint lies within the PDA's active aperture, efficient coupling is achieved. Even in the presence of lateral displacement misalignment, the PDA maintains stable reception, providing robust optical alignment tolerance in previous work.

At the transmitter side, the optical signal first propagates through 25 km of single mode fiber (SMF) and is then collimated into free space by a fiber collimator. After free space propagation, a condenser lens collects and focuses the beam onto the PDA. To ensure full illumination of the photosensitive area, the interplay between free space propagation distance and the Gaussian beam waist must be considered. According to Gaussian beam propagation theory, the transverse field distribution of the Gaussian mode follows a Gaussian profile. The beam waist radius $w(z)$ is defined at the position where the intensity drops to 1/e^2 of the on axis maximum. The complex beam parameter is given by

$$\frac{1}{q(z)} = \frac{1}{R(z)} - \frac{\lambda}{\pi w^2(z)} i \tag{1}$$

where $R(z)$ is the radius of curvature of the wavefront and λ is the optical wavelength. Beam propagation through an optical system is modeled via the ABCD matrix. For an input parameter q_0, the output beam parameter is:

$$q(z) = \frac{Aq_0 + B}{Cq_0 + D} \tag{2}$$

where A, B, C, D are the elements of the optical transfer matrix. By cascading multiple optical elements, the output beam waist radius and position can be calculated from the overall transfer matrix. When the beam passes sequentially through multiple optical elements, the overall transfer matrix is:

$$M = M_n M_{n-1} \ldots\ldots M_2 M_1 = \begin{bmatrix} A & B \\ C & D \end{bmatrix} \tag{3}$$

The corresponding output beam radius is:

$$w = \sqrt{A^2 w_0^2 + \frac{B^2 \lambda^2}{\pi^2 w_0^2 n_0^2}} \tag{4}$$

where w_0 is the input waist radius and n_0 is the refractive index of the incident medium. We use the theory to set tolerances for both the free space and focusing parts so the focused spot fits the element photosensitive area. Since the collimator and focusing optics are aspheric, the optical system was modeled and simulated in Ansys Zemax OpticStudio [23]. In the simulation, the collimated incident beam diameter was set to waist radius 1.5 mm and a focusing lens with a focal length of 30 mm was used to direct the beam onto the PDA surface. The distance between the collimator and the condenser lens d and the distance from the condenser lens to the PDA z are swept to quantify their impact on the output waist. The simulation results are shown in Fig. 1. When d was varied from 0mm to 50mm, the output waist radius only changed from 10.8886 μm to 10.88862 μm, a difference too small to significantly affect system performance. In contrast, the distance z predominantly governs the beam waist at the photodetector.

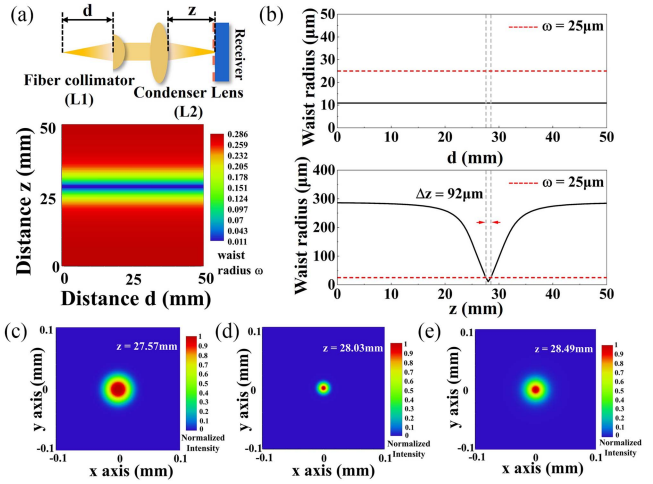

Fig. 1. (a) The effect on the beam waist radius for beam spot size on the PDA surface when moving the collimator to condenser lens distance d and the condenser lens to PDA distance z. (b) The ranges of d and z that keep the focused spot in the PDA valid photosensitive area (w<25 μm). The z axis displacement is 92 μm. (c), (d), (e) Normalized intensity on the PDA at different z. Illustrating the Gaussian beam spot before focus, at focus and post focus point.

Ray tracing simulations were further conducted to analyze beam spot size at different incident positions on the PDA. With an initial beam waist radius of 5.2 μm at the collimator, the condenser lens focused the beam on the PDA. As the beam position z was shifted from 0 mm (close to the condenser lens) to 28 mm (near the focus) and up to 50 mm (far from focus), the Gaussian spot profile was tracked. To ensure proper illumination, the spot radius on the PDA must be less than the element radius. The simulation results shown in Fig. 1(b) indicate that this condition is satisfied within a tolerance window of z from

27.57 mm to 28.49 mm. The spacing z directly affects the spot position on the PDA, as shown in Fig. 1(c), (d), and (e). At the $z = 27.57$ mm, the beam has not fully converged but the Gaussian waist radius is 24.5 μm, which is below the 25 μm element radius, the spot lies entirely within the photosensitive area, so the incident light is collected and converted to photocurrent. At $z = 28.03$ mm, the spot reaches its minimum gaussian waist with the highest energy density, which waist radius is 10.9 μm. Increasing to $z = 28.49$ mm places the photodetector after focus, so the spot size expand and the peak intensity drops. But the gaussian waist radius is still 24.4 μm, which remains inside the photosensitive area.

The spot size varies almost symmetrically about the focus and the nearly circular equal intensity contours indicate small aberrations and good focusing quality. The trend matches the waist versus z curve. As long as z stays within this range, the spot radius remains smaller than the element radius of 25 μm. Therefore, the energy is collected and the photocurrent remains essentially constant. It achieves practical robustness against z axis displacement. The results revealed that the 92 μm positional offset of the beam center was still fully contained within the 10-element PDA photosensitive region, thereby confirming robust coupling tolerance.

III. The Optical Alignment Tolerance Measurements

When the PDA is positioned near the focal plane of the condenser lens and the focused spot lies within the photosensitive area, the incident optical power is collected efficiently and the photocurrent reaches its maximum. The photodetector does not need to be located exactly at the point of minimum spot size. The PDA has a relatively large photosensitive area, the incident optical power is effectively collected and the photocurrent reaches its maximum. If the PDA is moved outside this range, the spot will grow and the irradiance at the surface will decrease, causing the photocurrent to drop accordingly. It provides a practical rule for setting the optimal coupling position. During z axis displacement, if the spot diameter remains below 50 μm, the photocurrent is essentially unchanged. The photodetector does not need to be located exactly at the point of minimum spot size.

Therefore, to ensure correct PDA position in the practical experiment, we evaluated the optical alignment tolerance of the PDA to highlight the advantage of receiving the beam in RoFSO communication system. We measured the z axis optical alignment tolerance across the 10 elements. A tunable laser source (Santec TSL-510), a power meter (Newport 1936-R), a semiconductor parameter analyzer (Keithley 4100) and a microstage were used to illuminate the PDA, record the generated photocurrent and estimate alignment tolerance. In the RoFSO design, we first focus on the optical unit excluding the RF setup. The fiber collimator and the condenser lens focused the beam onto the central 10 elements matrix of the PDA. Adjacent elements along x axis were spaced 100 μm (edge to edge) and the PDA exhibited no response when the beam illuminated inter element insensitive regions. Guided by ray trace simulations, we setup the PDA based optical module and characterized key optical metrics. The photocurrent varied and the corresponding location was recorded.

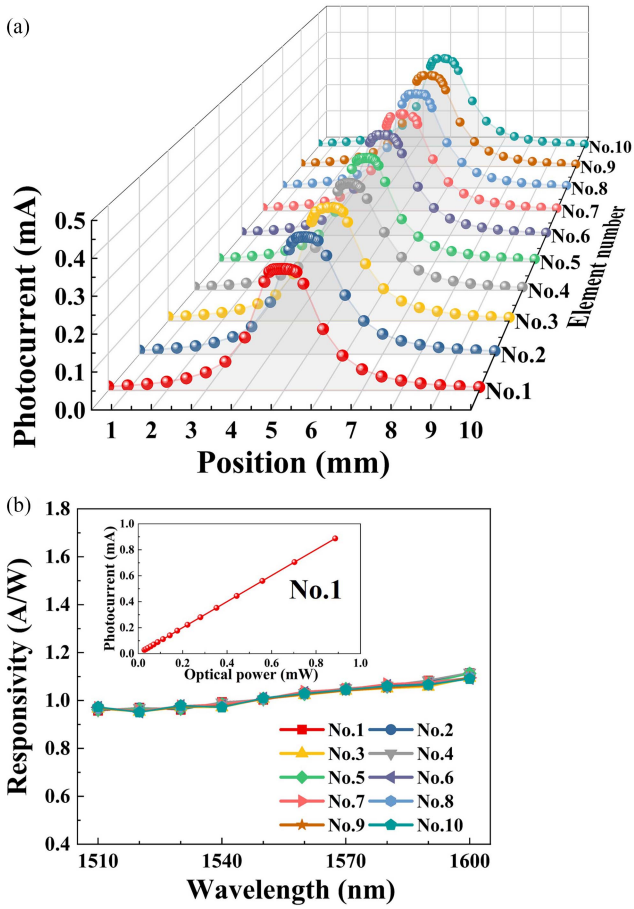

Fig. 2. (a) The z axis optical alignment profile for the 10-element PDA. (b) The responsivity between each element in the PDA. Inset: The P-I (power-photocurrent) characteristics of Element No.1 at -5 V bias.

The z axis photocurrent distribution profile was measured at the center of the PDA under beam spot conditions shown in Fig. 2(a). The photocurrent remained constant as long as the spot diameter on the PDA was smaller than its 50 μm photosensitive area. It creates a broad flat region in the I–z curve, indicating strong tolerance to axial misalignment. The optimal operating point should therefore be set near the center of the region. The z-axis alignment tolerance varies across the array, with a maximum of 76 μm and an average of 65 μm for the 10 elements. This measured tolerance is slightly lower than the theoretical value of 92 μm obtained when the PDA is positioned at the ideal focus plane. The discrepancy is attributed to mechanical imperfections in the setup. A small pitch angle error in the lens mount causes lateral beam offset at the receiver and the micro stage exhibits slight unintended motion when switching between elements during alignment, shifting the PDA away from the optimal focus plane. These mechanical limitations can be minimized in the implementations through improved mounting precision and more stable positioning systems. Despite minor mechanical imperfections, the measured spot sizes and positions indicate reliable RoFSO reception within the PDA and high tolerance to small axial offsets. Overall, the designed FSO receiver efficiently couples the focused Gaussian spot onto the PDA while maintaining robustness to position variations.

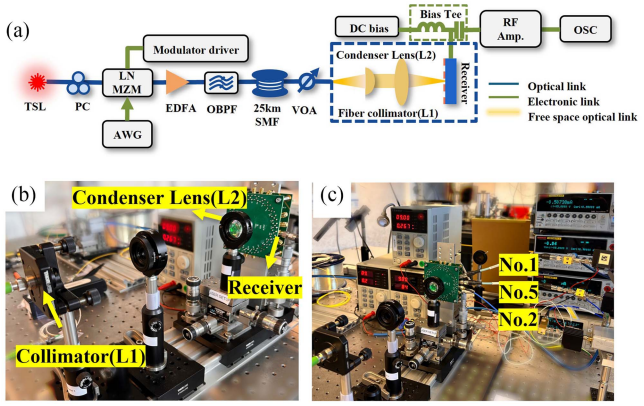

Fig. 3. (a) Experimental setup for RoFSO communication using PDA as receiver. The blue, green and orange lines represent the electrical, optical and free space optical links, respectively. (b) The free space light direct coupling in the receiver. (c) The different elements in the PDA measured at the same time. TSL: tunable laser; PC: polarization controller; LN MZM: lithium niobate Mach-Zehnder modulator; EDFA: erbium-doped fiber amplifier; OBPF: optical band pass filter; 25 km SMF: 25 km single mode fiber; VOA: variable optical attenuator; AWG: arbitrary waveform generator; RF Amp.: RF amplifier; OSC: oscilloscope.

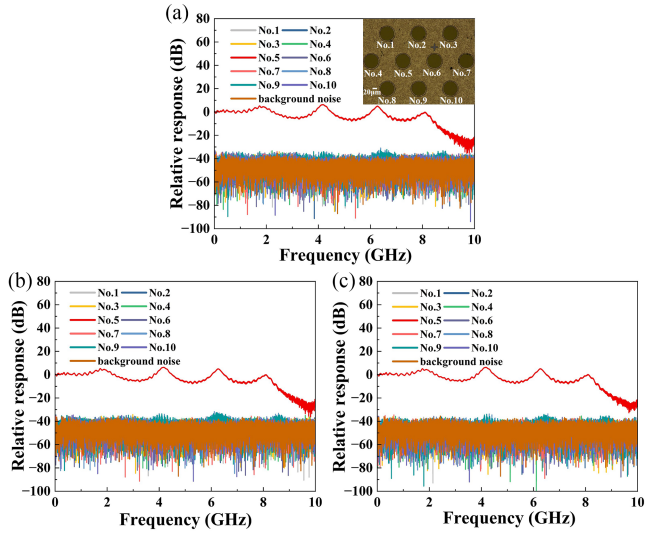

Fig. 4. The wavelength dependent crosstalk between Element No.5 and the nearest and secondary neighboring elements were measured at different wavelength: (a) 1510 nm; (b) 1550 nm; (c)1600 nm. Inset: The arrangement of the 10 selected elements in the PDA.

We measured the responsivity via P-I (optical power-photocurrent) curves of every photodetector over 1510–1600 nm at a reverse bias of 5 V and compared the results across wavelength, using beam conditions optimized for maximum photocurrent. The responsivity is the ratio between input optical power and output photocurrent. The average responsivity exceeds 1.01 A/W under free space reception, indicating that each photodetector in the array operates properly. Fig. 2(b) also shows the photocurrent response of Element No.1 as the input optical power is varied from 0.03 mW to 0.88 mW, confirming the expected P-I scaling under operating conditions.

IV. Transmission Experiments: Results and Discussion

In RoFSO systems, minimizing crosstalk is critical for preserving a high signal to noise ratio (SNR, Q-factor), a low bit error rate (BER) and manageable digital signal processing (DSP) complexity at the receiver. The challenge is particularly pronounced in high frequency, multi-channel optoelectronic systems, where interference risks are exacerbated by close channel spacing and compact packaging. After the optical signal is converted into a high frequency electrical signal by the photodetector, additional electrical crosstalk may still occur during transmission within the packaging circuitry. Fig. 3(a), (b) and (c) show the experimental setup for a RoFSO communication system using the PDA as receiver for space diversity reception. It employs a single optical input with multiple electrical outputs and demonstrated its effectiveness for short distance RoFSO communication. On the transmit side, high data rate pseudo random bit sequence (PRBS) of $2^{15}-1$ non return to zero (NRZ) and PAM-4 signals were generated by an arbitrary waveform generator (AWG), then converted to the optical domain using a lithium niobate intensity modulator driven by a 1550 nm laser. The optical signal was sent through 25 km of fiber to emulate an analog long communication transmission and then launched into a short range FSO path of 0.35 m (limited by the rail length). The transmitter used an aspheric objective collimator ($f = 15.58$ mm), which transmits a 3.0 mm beam. A condenser lens ($f = 30$ mm) at the receiver focused this beam to a spot size below 50 μm on the PDA surface. The mechanical functions like beam tracking and an active alignment system were ruled out. At the receiver, the PDA was packaged with RF coaxial connectors. The 10 selected elements in the center were fan out with a small through hole for back illumination. The electrical output from the selected PD was passed through a bias tee and amplified by an amplifier (23dB SHF S807). Finally, the output was observed on a high speed oscilloscope (Keysight DCA-X).

A. Small Signal Radio Frequency Measurements: Crosstalk

The relative opto-electrical frequency response (S21) of the central channel (No.5) was characterized using a vector network analyzer (VNA), with its nearest (No.1, No.2, No.4, No.6, No.8 and No.9) and secondary (No.3, No.7 and No.10) adjacent channels serving as the test subjects for crosstalk assessment, as shown in Fig. 4. The measurement results indicate that both the nearest and secondary neighboring channels fall to the noise floor, at levels comparable to the baseline noise. It was estimated to be approximately -30 dB below the main signal (No.5) at 2.8 GHz (3 dB bandwidth). This confirms that crosstalk is negligible and that multiple channels can reliably transmit signals in parallel. Although some response peaks around 1.8 GHz, 4.1 GHz and 6.4 GHz can be observed in the frequency response, it might be caused by impedance mismatch. Fig. 4 shows the opto-electrical frequency response of Element No.5 and the crosstalk from its neighboring elements at 1510 nm, 1550 nm and 1600 nm. The results demonstrate that both the main channel response and the crosstalk characteristics

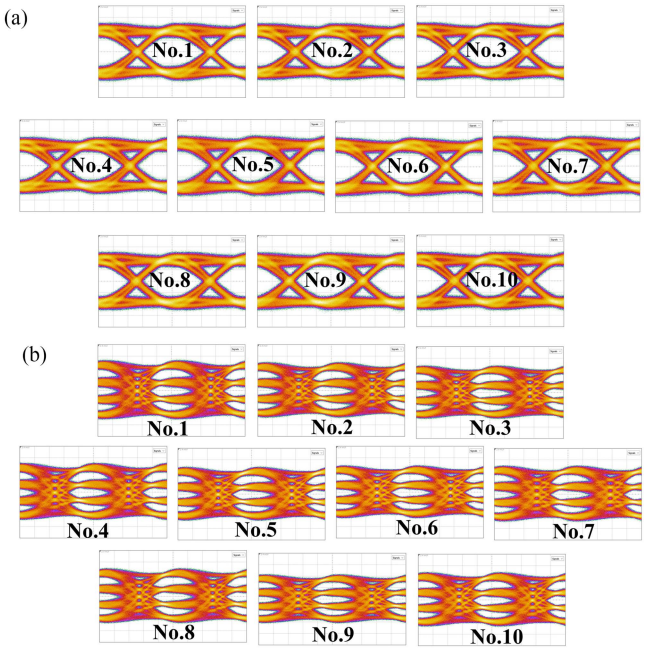

Fig. 5. (a) Measured 100 Gbps (10 × 10 Gbps) NRZ eye diagrams at −5 V for 10 elements in the RoFSO transmission. (b) Measured 100 Gbps (10 × 10 Gbps) PAM-4 eye diagrams at −5 V for 10 elements in the RoFSO transmission.

remain unchanged across this 90 nm bandwidth. The crosstalk from nearest and secondary neighboring channels consistently reaches the measurement noise floor at approximately −30 dB below the main signal at 2.8 GHz (3 dB bandwidth), independent of wavelength. The consistent −30 dB crosstalk level across the C-band validates the robustness of our PDA design for broadband RoFSO applications. However, we confirmed that they have no impact on the high data rate RoFSO communication demonstration presented in eye diagram and bit error rate assessments. In the RoFSO systems, the beam required alignment within a 10-element PDA area via an optical condenser lens already demonstrating high alignment robustness. The performance of the receiver was further verified by measuring large signal eye diagrams. Transmission was measured for various space diversity combining configurations with the optical beam spot positioned at the center of the array to ensure uniform illumination.

B. Eye Diagram and Bit Error Rate Assessments

Fig. 5 shows the schematic for high speed NRZ and PAM-4 eye diagram measurements. Each element was measured independently to demonstrate individual channel performance and uniform array characteristics. With a photocurrent of −0.3 mA, clear open eye diagrams for 10 Gbps NRZ modulation were obtained at −5 V. The minimum output amplitude exceeded 15 mV and was amplified to approximately 100 mV, average eye height is 84 mV. For the 10 Gbps NRZ signals at −5 V, the PDA elements achieved the following Q-factors: 7.14, 7.43, 7.23, 7.58, 7.88, 7.39, 7.40, 7.48, 7.45, 7.03, respectively. The relatively consistent Q-factor values across the array indicate

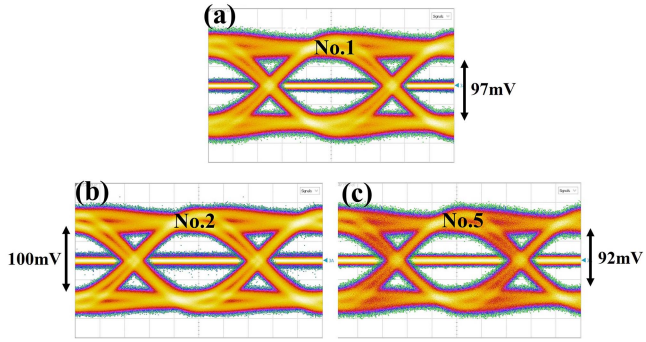

Fig. 6. Channel isolation performance measurement of the RoFSO system. The eye diagrams of channels No.1, No.2 and No.5 in individually worked, with signal amplitudes of 97 mV, 100 mV and 92 mV, respectively.

uniform responsivity and stable optical coupling among the PDA elements. Although the initial free space transmission experiment was limited to 0.35 m due to the rail length limit, the system is intended for indoor applications. Extrapolation based on the fiber collimator parameters suggests that extending the transmission range beyond 1 m is feasible with the current collimator. Its low beam divergence maintains a compact spot size over meter scale propagation thereby ensuring stable transmission quality. For indoor short transmission path length, atmospheric turbulence is negligible, the primary practical considerations are mechanical alignment stability and high data rate transmission performance. The employed collimator provides a sufficiently small beam divergence, maintaining a compact beam spot size over 1 m longer distances and thus ensuring stable transmission quality. The BER was subsequently measured for each PDA element to quantitatively evaluate the transmission quality and verify consistency across the array. To further verify the system's potential for RoFSO applications, eye diagram measurements were also performed using the PAM-4 modulation format. A 10 Gbps PAM-4 signal was applied to the 10-element PDA and processed with transmitter equalization. The resulting eye diagram is shown in Fig. 5(b). The eye diagram measurement results indicate that the proposed PDA is qualified as the receiver of a 100 Gbps (10 × 10 Gbps) communication system at 1550 nm wavelength.

The primary challenge facing RoFSO systems lies in the effective suppression of inter-channel crosstalk, which directly affects system signal integrity and scalability. To verify the performance of the designed RoFSO using PDA as receiver, crosstalk was measured in the eye diagrams for three independent spatial channels transmitted simultaneously. The three RF output signals were measured using a four channels high speed oscilloscope. Based on the measurement results of the RoFSO shown in the Fig. 6, the three spatial channels (No.1, No.2 and No.5) demonstrated excellent signal transmission performance and channel isolation characteristics. As shown in Fig. 6(a), when the No.1 channel was activated and transmitted a 10 Gbps NRZ signal, the eye diagram presented a clear eye opening with an eye height of 97 mV, eye width of 77.36 ps, minimal jitter and root mean square (RMS) jitter of 3.772 ps. Similarly, in Fig. 6(b) and (c), the No.2 and No.5 channels transmitted signals and both

TABLE I
THE COMPARISON OF DIFFERENT INDOOR ROFSO SYSTEMS

Ref.	Channel number	Bit rate (Gbps)	Fiber link distance (km)	Free space distance (m)	Modulation format	Tracking required
[24]	1	10	—	0.1	OOK	no mechanical tracking
[25]	3	10	—	0.15	OOK	no mechanical tracking
[26]	2	10	5.6	2	OOK	MEMS-based steering mirrors
[27]	12	40	——	2.1	PAM4	Active tracking
[28]	2	10	0.053	0.5	BPSK	No beam tracking
[20]	4	2	5	1	QPSK	No beam tracking
This work	10	10×10	25	0.35	OOK&PAM4	No beam tracking

exhibited good signal integrity, with eye heights of 100 mV and 92 mV, eye widths of 75.08 ps and 75.58 ps, RMS jitter of 4.152 ps and 4.070 ps, respectively, when different channels were activated. It is worth noting that during the individual operation of each channel, the crosstalk level of the other two inactive channels was effectively suppressed below approximately 6 mV, demonstrating the excellent inter channel isolation of the RoFSO system. The results showed that the RoFSO system maintained stable eye diagram patterns over a transmission SMF distance of 25 km.

The BER performance of the space diversity system was evaluated across different receiver elements to investigate the relationship between BER and output photocurrent. Fig. 7(a) shows the BER measurement results for the 10 selected central elements operating at 10 Gbps with a −5 V bias. The mechanical positioning errors during beam realignment, combined with the Gaussian beam intensity profile will result in different received optical power and signal to noise ratio (SNR) for each element. As the input optical power varies, the photocurrent changes proportionally and BER performance degrades accordingly. The element to element variations in frequency response lead to varying degrees of signal distortion. For element No.1, a minimum optical power of −4.6 dBm corresponds to a photocurrent of −0.35 mA. All 10 elements achieved a BER $<1 \times 10^{-12}$, confirming uniform and reliable detection performance of the receiver. To assess the bandwidth limitation and highest speed transmission capability of the receiver, a PRBS signal of $2^{15}-1$ was applied over a range of data rates from 8 Gbps to 20 Gbps using an externally modulated laser operating at 1550 nm. Fig. 7(b) shows the in plane BER distribution of Element No.1. The receiver frequency response indicates that the ability of the receiver to transmit high frequency components sharply declines around 8 GHz. The BER experiences a sudden rise at 16 Gbps because the frequency component of the NRZ signal exceeds the receiver's bandwidth limit. This bandwidth-limited regime makes reliable bit detection impossible even at higher optical power. The attenuated high frequency components result in pulse broadening and severe inter-symbol interference (ISI), where energy from adjacent bits overlaps and degrades the eye opening. The BER experiences a sudden rise at 16 Gbps. When the bit rate exceeds the bandwidth, the high frequency components are attenuated, causing high BER. This provides a reliable technical solution for high density optical interconnection communication systems. The system ensures signal quality of each independent channel while increasing transmission capacity, with a total system capacity reaching 100 Gbps. To the best of our knowledge, as summarized in Table I, this work demonstrates

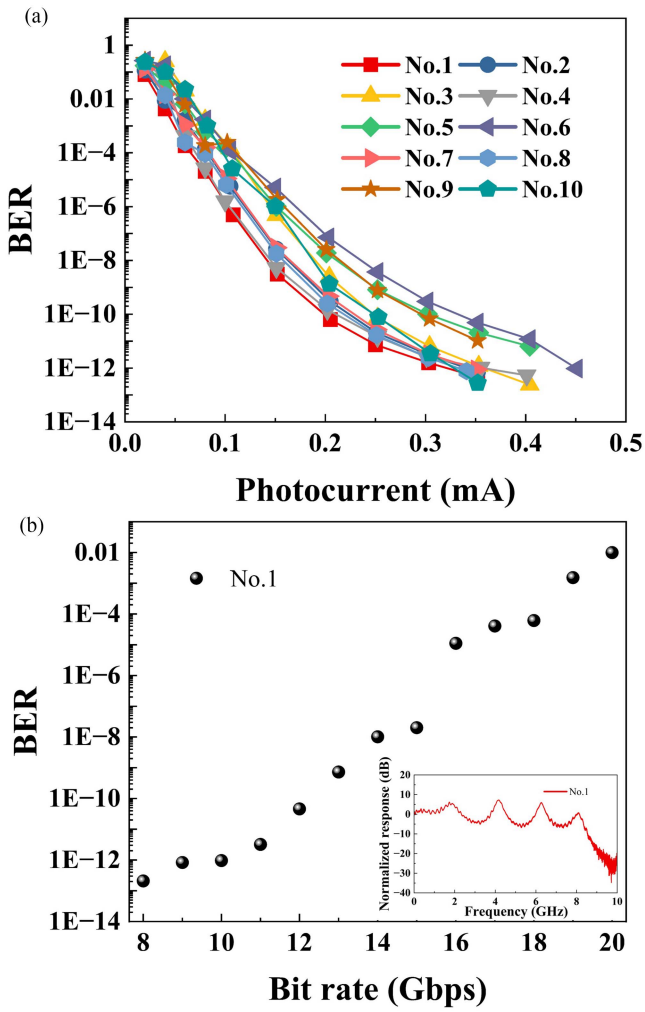

Fig. 7. (a) The performance of 10 elements in the receiver at 10 Gbps NRZ for bit error rate measurement. (b) BER of Element No. 1 measured at different bit rates and corresponding bandwidths.

one of the highest aggregate transmission capacities for short range RoFSO systems under comparable free space and fiber link conditions. While this work demonstrates NRZ and PAM-4 modulation formats, the proposed PDA-based receiver architecture is inherently compatible with coherent detection schemes. Each PDA element can serve as the input to an independent receiver. The optical alignment robustness and space diversity capabilities demonstrated herein would equally benefit coherent RoFSO implementations.

V. Conclusion

In this work, the implementation of RoFSO communication using space diversity reception based on a PDA receiver with high optical alignment robustness was demonstrated. The receiver was configured with a single optical condenser lens and a newly developed PDA, exhibiting -30 dB crosstalk between elements. A large alignment tolerance of 65 μm along the z axis of the receiver was achieved without mechanical beam tracking or active alignment functions. In the total 100 Gbps NRZ and PAM-4 PDA demonstrations, a BER $<1 \times 10^{-12}$ was obtained for the selected 10 elements when the beam was aligned to the center of the PDA. Clear and open eye diagrams of NRZ and PAM-4 were shown. To verify the RoFSO application, three channel transmission was demonstrated with space diversity for single input and multiple outputs over a 25 km distance. The aligned multi element design in the receiver proves suitable not only for mitigating optical alignment challenges but also for enabling multiple output digital signal processing in RoFSO receivers. This high performance provides a reliable solution for indoor short range optical transmission networks and shows strong potential for applications including 5G and 6G fronthaul and backhaul in indoor deployments, data center interconnects and high performance computing systems to address future ultra high capacity transmission requirements.

Acknowledgment

The authors thank Ing.Steven Verstuyft, Ing.Hasan Salmanian and Dr. Tingting Zhai for their help and support.

References

[1] K. P. Kalinin et al., "Analog optical computer for AI inference and combinatorial optimization," *Nature*, vol. 645, pp. 1–8, 2025.
[2] K. Liu et al., "High-speed 0.22 THz communication system with 84 Gbps for real-time uncompressed 8K video transmission of live events," *Nature Commun.*, vol. 15, no. 1, 2024, Art. no. 8037.
[3] D. C. Nguyen et al., "6G Internet of Things: A comprehensive survey," *IEEE Internet Things J.*, vol. 9, no. 1, pp. 359–383, Jan. 2022.
[4] A. Gupta and R. K. Jha, "A survey of 5G network: Architecture and emerging technologies," *IEEE Access*, vol. 3, pp. 1206–1232, 2015.
[5] M. E. Morocho-Cayamcela, H. Lee, and W. Lim, "Machine learning for 5G/B5G mobile and wireless communications: Potential, limitations, and future directions," *IEEE Access*, vol. 7, pp. 137184–137206, 2019.
[6] C.-X. Wang et al., "On the road to 6G: Visions, requirements, key technologies, and testbeds," *IEEE Commun. Surveys Tut.*, vol. 25, no. 2, pp. 905–974, Secondquarter 2023.
[7] M. Van den Hout et al., "Reaching the pinnacle of high-capacity optical transmission using a standard cladding diameter coupled-core multi-core fiber," *Nature Commun.*, vol. 16, no. 1, 2025, Art. no. 3833.
[8] K. Srivastava and N. Bhatia, "An all-fiber multimode interference device for power splitting in few mode fiber networks," *J. Lightw. Technol.*, vol. 43, no. 2, pp. 799–808, Jan. 2025.
[9] Y. Xiong et al., "Ultracompact multicore fiber de-multiplexer using an endface-integrating graphene photodetector array," *ACS Photon.*, vol. 9, no. 5, pp. 1808–1813, 2022.
[10] A. Bekkali, H. Fujita, and M. Hattori, "Fiber-to-fiber FSO system with advanced VCM controlled laser beam pointing and tracking," in *Proc. Opt. Fiber Commun. Conf. Exhib.*, 2021, pp. 1–3.
[11] T. Yoshida et al., "Full C-band two-dimensional beam-steering silicon PIC and 15.36-Tbit/s free-space optical transmission," in *Proc. Opt. Fiber Commun. Conf. Exhib.*, 2025, pp. 1–3.
[12] H. Chun, A. Gomez, C. Quintana, W. Zhang, G. Faulkner, and D. O'Brien, "A wide-area coverage 35 Gb/s visible light communications link for indoor wireless applications," *Sci. Rep.*, vol. 9, no. 1, 2019, Art. no. 4952.
[13] C.-H. Yeh et al., "1.7 to 2.3 Gbps OOK LED VLC transmission based on 4 $\times$ 4 color-polarization-multiplexing at extremely low illumination," *IEEE Photon. J.*, vol. 11, no. 4, Aug. 2019, Art. no. 7904206.
[14] R. Bian, I. Tavakkolnia, and H. Haas, "15.73 Gb/s visible light communication with off-the-shelf LEDs," *J. Lightw. Technol.*, vol. 37, no. 10, pp. 2418–2424, May 2019.
[15] S. M. Walsh et al., "Demonstration of 100 Gbps coherent free-space optical communications at LEO tracking rates," *Sci. Rep.*, vol. 12, no. 1, 2022, Art. no. 18345.
[16] V. W. S. Chan, "Free-space optical communications," *J. Lightw. Technol.*, vol. 24, no. 12, pp. 4750–4762, 2006.
[17] M. A. Khalighi and M. Uysal, "Survey on free space optical communication: A communication theory perspective," *IEEE Commun. Surveys Tuts.*, vol. 16, no. 4, pp. 2231–2258, Fourthquarter 2014.
[18] K. Kazaura, K. Wakamori, M. Matsumoto, T. Higashino, K. Tsukamoto, and S. Komaki, "RoFSO: A universal platform for convergence of fiber and free-space optical communication networks," *IEEE Commun. Mag.*, vol. 48, no. 2, pp. 130–137, Feb. 2010.
[19] T. Umezawa et al., "400-Gbps space division multiplexing optical wireless communication using two-dimensional photodetector array," in *Proc. Eur. Conf. Opt. Commun.*, 2018, pp. 1–3.
[20] H. Huang et al., "A multi-access RoFSO communication system incorporating a microwave photonic channel aggregator," *J. Lightw. Technol.*, vol. 43, no. 5, pp. 2184–2191, Mar. 2025.
[21] T. Koonen, K. Mekonnen, F. Huijskens, Z. Cao, and E. Tangdiongga, "Novel broadband OWC receiver with large aperture and wide field-of-view," in *Proc. Eur. Conf. Opt. Commun.*, 2020, pp. 1–4.
[22] Y. Yunjie et al., "Optical signal acquisition using an alignment robust receiver based on photodetector array," *Opt. Lett.*, vol. 50, no. 23, pp. 7199–7202, 2025.
[23] ZEMAX, "Ansys Zemax Opticstudio," 2025. [Online]. Available: https://www.ansys.com/zh-cn/products/optics/ansys-zemax-opticstudio
[24] Y. Atsumi et al., "Broadband port-selective silicon beam scanning device for free-space optical communication," *IEICE Trans. Electron.*, vol. E106.C, no. 11, pp. 739–747, Nov. 2023.
[25] Q. You, D. Chen, X. Xiao, and S. Yu, "10 Gb/s free space optical interconnect with broadcasting capability enabled by a silicon integrated optical phased array," *Chin. Opt. Lett.*, vol. 19, no. 12, Dec. 2021, Art. no. 120602.
[26] K. Wang, A. Nirmalathas, C. Lim, K. Alameh, and E. Skafidas, "Full-duplex gigabit indoor optical wireless communication system with CAP modulation," *IEEE Photon. Technol. Lett.*, vol. 28, no. 7, pp. 790–793, Apr. 2016.
[27] Z.-K. Weng et al., "High-mobility 40-Gbps free-space optical link by a three-stage high-speed beam stabilizer and 2-D photodetector array based diversity reception," *Opt. Exp.*, vol. 33, no. 8, pp. 16820–16832, 2025.
[28] T. Su et al., "Demonstration of free space coherent optical communication using integrated silicon photonic orbital angular momentum devices," *Opt. Exp.*, vol. 20, pp. 9396–9402, Apr. 2012.